1 # Intraseasonal variability of the South Vietnam Upwelling, South

2 # China Sea: influence of atmospheric forcing and ocean intrinsic

3 # variability.

5 Marine Herrmann[1*], Thai To Duy[2], Claude Estournel[1]

6 [1] Université de Toulouse, LEGOS (IRD/CNES/CNRS/UPS), Toulouse, France, 31400 Toulouse, France

7 [2] Institute of Oceanography (IO), Vietnam Academy of Science and Technology (VAST), Nha Trang, Vietnam

8 *Correspondence to :* Marine Herrmann (marine.herrmann@ird.fr)

9 **Short summary**

10 The South Vietnam Upwelling develops in summer along and off the Vietnamese coast. It brings cold and nutrient-
11 rich waters to the surface, allowing photosynthesis essential to marine ecosystems and fishing resources. We show
12 here that its daily variations are mainly due to the wind, thus predictable, in the southern shelf and coast regions.
13 However, they are more chaotic in the offshore area, and especially in the northern area, due to the influence of
14 eddies of a highly chaotic nature.

15    **Abstract**

16    The South Vietnam Upwelling (SVU) develops off the Vietnamese coast (South China Sea) during the southwest

17    summer monsoon over four main areas: the northern coastal upwelling (NCU), the southern coastal upwelling

18    (SCU), the offshore upwelling (OFU) and the shelf off the Mekong River mouth (MKU). An ensemble of ten

19    simulations with perturbed initial conditions were run with the fine-resolution SYMPHONIE model (1 km

20    inshore) to investigate the daily to intraseasonal variability of the SVU and the influence of the ocean intrinsic

21    variability (OIV) during the strong SVU of summer 2018.

22    The intraseasonal variability is similar for SCU, MKU and OFU, driven to the first order by the wind variability.

23    MKU and SCU are induced by stable ocean dynamics (the northeastward then eastward boundary current) and

24    have very little chaotic variability. The OIV has a stronger influence on OFU. In July, OFU mainly develops along

25    the northern flank of the eastward jet. The influence of OIV is strongest and related to the chaotic variability of

26    the meridional position of the jet. In August this position is stable and OFU develops mainly in the area of positive

27    wind curl and cyclonic eddies north of the jet. The influence of OIV, weaker than in July, is related to the

28    organization of this mesoscale circulation. NCU shows a behavior different from what observed in the other areas.

29    In the heart of summer, a large-scale circulation formed by the eastward jet and eddy dipole is well established

30    with an alongshore current preventing NCU development. In early and late summer, this circulation is weaker,

31    allowing a mesoscale circulation of strongly chaotic nature to develop in the NCU area. During those periods, the

32    OIV influence on NCU is very strong and related to the organization of this mesoscale circulation: NCU is favored

33    (annihilated) by offshore-oriented (alongshore) structures.

34

35    **1.  Introduction**

36    The summer general circulation in the central South China sea is largely induced by the prevailing southwest

37    monsoon winds (Wang et al., 2004; Wyrtki et al., 1961). It is characterized by the development off the central

38    Vietnamese coast of an anticyclonic (AC) gyre in the south and a cyclonic (C) gyre in the north (forming an eddy

39    dipole referred to as the ACC dipole) and of the South Vietnam upwelling, hereafter referred to as the SVU, that

40    develops over four main areas. First, the convergence of two gyres creates an eastward jet departing from the

41    southern part of the central coast of Vietnam between 11°N and 12°N. This convergence gives rise to an Ekman

42    current-induced coastal upwelling (Dippner et al., 2007; Chen et al., 2012), hereafter referred to as SCU. Second,

43    Ekman pumping-induced upwelling (OFU hereafter) develops offshore in the area of strong positive wind and

44    surface current vorticity (Liu et al., 2012; Da et al., 2019; Ngo and Hsin, 2021). Third, recent studies have revealed

45    that coastal upwelling (NCU hereafter) can develop along the northern part of the central Vietnamese coast (Da

46    et al., 2019; Ngo and Hsin, 2021; To Duy et al., 2022). Last, To Duy et al. (2022) showed for the first time that

47    upwelling develops off the Mekong Delta behind Con Dao islands (see Fig. 1b, MKU hereafter). SVU participates

48    to the nutrient enrichment of the surface layer, hence plays an important role in the biological productivity and in

49    the halieutic resources of the region (Bombar et al., 2010; Liu et al., 2012; Loick-Wilde et al., 2017; Lu et al.,

50    2018; Loisel et al., 2017). Some authors also showed that the SVU may influence the functioning of local and

51    regional climate (Xie et al., 2003; Zheng et al., 2016). Understanding precisely the functioning and variability of

52    the SVU and its response to long-term changes is therefore an important issue.

The interannual variability of the SVU has been investigated in numerous previous studies. In the SCU, OFU and MKU regions, the interannual variability of summer wind intensity is related to and in phase with the intensity of the summer monsoon, and is the main driver of the interannual variability of upwelling intensity (Wang et al., 2006; Chen et al., 2014; Li et al., 2014; Da et al., 2019; Ngo and Hsin, 2021; To Duy et al., 2022). ENSO (El Niño Southern Oscillation) also impacts the upwelling in those regions, due to its influence on summer monsoon wind (Wang et al., 2006; Kuo et al., 2004; Loick-Wilde et al., 2017; Da et al., 2019). Some studies (Li et al., 2014; Da et al., 2019) then revealed that ocean intrinsic variability (OIV) influences the interannual variability of the eastward jet and of the OFU. OIV, as opposed to the forced variability, corresponds to the unpredictable part of ocean variability, not induced by the variability of external forcing factors but by the chaotic behavior of ocean dynamics. Most studies have shown that mesoscale to submesoscale structures are a major source of OIV (Penduff et al., 201; Sérazin et al., 2016; Waldman et al., 2018; Da et al. 2019). This influence of OIV is related to the spatial distribution of summer averaged surface current vorticity associated with eddies: cyclonic (anticyclonic) eddies located in the area of positive wind stress curl enhance (weaken) the Ekman pumping-induced OFU. The interannual variability of NCU shows a completely different behavior. Ngo and Hsin (2021) and To Duy et al. (2022) concluded that wind conditions favorable to SCU, MKU and OFU were unfavorable to NCU, and vice versa. To Duy et al. (2022) moreover showed that the influence of wind is weaker for NCU than for the other areas. In contrast, the influence of circulation, in particular of the spatial organization of the chaotic submesoscale to mesoscale circulation that prevails over the area, was found to be stronger: on a seasonal average, NCU is inhibited when alongshore currents prevail, and enhanced when offshore circulation prevails.

The daily to intraseasonal variability of the SVU was much less studied. Available studies, all based on satellite data, focused on the SCU and OFU. Xie et al. (2007) showed that the upwelling in those areas does not develop smoothly during the summer, but shows a strong intraseasonal variability related to the wind variability and Madden Julian Oscillation (MJO). They suggested that SVU experiences two to four events of development and decay during the summer, in response to the wind fluctuations. Isoguchi and Kawamura (2006) and Liu et al. (2012) confirmed respectively for the period 2000-2002 and for summer 2007 that the MJO is a strong driver of the events of southwesterly wind intensification within the season and of the resulting upwelling. They moreover revealed the effect of tropical storms that can reinforce the southwesterly wind, hence the SVU.

To better understand the functioning and variability of the SVU, it is therefore necessary to investigate in detail the functioning of its daily to intraseasonal variability over its four areas of development (SCU, NCU, OFU and MKU) and to identify the driving factors. Previous studies mentioned above revealed the role of wind for SCU and OFU, which should be examined for the other areas. The role of OIV in the interannual variability of the upwelling, related to mesoscale circulation and eddies in the coastal and offshore area, was highlighted for OFU and suggested for NCU. It should be examined at the intraseasonal scale, and requires an ensemblist approach as used by Waldman et al. (2017a, 2018). Chen et al. (2012) also showed from idealized simulations that tides and river plumes could be also involved in SVU variability, however, to our knowledge, only very few models used for the SVU study included the effect of tides, and none of them investigated their impact.

The present paper focuses on the daily to intraseasonal variability of the SVU over its four areas of development, examining in particular the role of atmospheric forcing, in particular wind, and the role of ocean dynamics and their intrinsic variability. The effect of tides and rivers will be examined in a future study. A fine-resolution

92  realistic model including tides and already presented and evaluated in To Duy et al. (2022) for the period 2009-

93  2018 is used. Ensemble simulations with perturbed initial conditions are performed to study the case of summer

94  2018, which was an exceptionally strong summer of upwelling for SCU, OFU and MKU (Ngo and Hsin, 2021;

95  To Duy et al., 2022).

96  The fine-resolution model and ensemble simulations and the definition of study areas, upwelling indicators and

97  OIV indicators are presented in Part 2. The intraseasonal variability of the oceanic circulation and of the SVU,

98  including the role of OIV, are examined respectively in Part 3 and Part 4. Results are summarized and future work

99  is discussed in Part 5.

100

101  **2.  Methodology**

102  **2.1.  The 3-D hydrodynamical ocean model SYMPHONIE**

103  To Duy et al. (2022) built a fine-resolution configuration of the 3-D ocean circulation model SYMPHONIE

104  (Marsaleix et al., 2008, 2019) over the Vietnam coastal region (VNC hereafter for VietNam Coast), based on a

105  horizontal polar grid with a resolution decreasing linearly seaward, from 1 km at the Vietnamese coast to 4.5 km

106  offshore, and with 50 vertical levels. They used the GEBCO_2014 dataset released in April 2015 at a 30 seconds

107  interval (~0.9 km) and available from www.gebco.net. We use exactly the same configuration here and show

108  VNC domain in Figure 1a,b. The atmospheric forcing is computed from the 3-hourly output of the European

109  Center for Medium-Range Weather Forecasts (ECMWF) 1/8° atmospheric analysis, distributed on

110  http://www.ecmwf.int. Initial and lateral ocean boundary conditions are prescribed from the daily outputs of the

111  global ocean 1/12° analysis PSY4QV3R1 distributed by the Copernicus Marine and Environment Monitoring

112  Service (CMEMS) on http://marine.copernicus.eu. The implementation of tides follows Pairaud et al. (2008, 2010)

113  and considers the 9 main tidal harmonics, provided by the 2014 release of the FES global tidal model (Lyard et

114  al., 2006). Freshwater discharge is provided for 36 river mouths. More details about the model, its configuration

115  and the forcings are provided in To Duy et al. (2022). They performed and evaluated a 10-year simulation over

116  the period 2009-2018, hereafter called LONG, showing that it reproduces realistically the temporal (seasonal to

117  interannual) and spatial variability of the SCS ocean dynamics and water masses. In the LONG simulation, a very

118  strong SVU developed during summer 2018, in particular due to strong July-August northeastward wind (To Duy

119  et al., 2022).

120  **2.2.  Ensemble simulations**

121  We performed an ensemble of ten simulations with perturbed initial conditions between January 1st, 2017 and

122  December 31st, 2018. For that we used ten different initial conditions for temperature, salinity, sea surface

123  elevation and currents fields. Most of the OIV develops at mesoscale (Sérazin et al., 2015, Waldman et al., 2018),

124  we therefore only perturbed the mesoscale field, following the same methodology as Waldman et al. (2017a,

125  2017b, 2018): for the ten simulations of the ensemble, the large-scale state of the initial field is identical, and the

126  small-scale of the initial field state differs. The common large-scale state is equal to the large-scale state of January

127  1st, 2017 of the LONG simulation, computed using a 100 km low-pass filter. For XX going from 09 to 18, the

128  small-scale state of January 1st, 20XX of the LONG simulation is computed using a 100 km high-pass filter. The

129 initial state of member XX of the simulation ensemble is then computed by adding this small-scale state to the
130 common large-scale state.

### 2.3. Definition of upwelling areas

132 Figure 1c,d shows the SST averaged over June-September (JJAS) 2018 for the ensemble average and for OSTIA
133 (Operational Sea Surface Temperature and Sea Ice Analysis) reanalysis outputs, available at
134 ftp://data.nodc.noaa.gov/pub/data.nodc/ghrsst/L4/GLOB/UKMO/OSTIA/. Simulated SST is in good agreement
135 with observations, showing a large area of colder surface water corresponding to the strong SVU that developed
136 during summer 2018. We show in Figure 1b,c,d the four boxes used by To Duy et al. (2022), that correspond to
137 the four main areas of SVU development: boxSC and boxNC for respectively the southern (SCU) and northern
138 (NCU) coastal upwelling, boxOF for the offshore upwelling (OFU), and boxMK for the upwelling offshore the
139 Mekong delta (MKU).

### 2.4. Indicators of upwelling intensity

141 We compute a SST-based index of upwelling intensity following exactly the same methodology as Da et al. (2019)
142 and To Duy et al. (2022). The daily upwelling index $UI_d$ is computed every day $t$ at each point (x,y) of the study
143 area that verifies $SST(x,y,t)<T_o$ as:

144 $$UI_d(x,y,t) = T_{ref} - SST(x,y,t) \text{ for (x,y,t) where SST(x,y,t)} < T_o \qquad (1)$$

145 The reference temperature $T_{ref}$ = 29.2°C is computed as the SST averaged over JJAS and over $boxT_{Ref}$, the area
146 east of the upwelling region that is the least impacted by upwelling (see Figure 1c,d), in the LONG simulation.
147 The threshold temperature under which upwelling occurs, $T_0$= 27.6°C, is defined as the optimal upwelling
148 threshold that covers the largest number of upwelling occurrences but avoids to include cold water horizontally
149 advected between upwelling areas.

150 For each box $boxN$, the daily intensity of upwelling integrated over $boxN$ is quantified at day $t$ by the daily
151 upwelling index $UI_{d,boxN}$, computed as:

152 $$UI_{d,boxN}(t) = \frac{\iint_{(x,y) in\ boxN\ so\ that\ SST(x,y,t)<T_0}(T_{ref}-SST(x,y,t)).dx.dy}{A_{boxN}} \qquad (2)$$

153 where $A_{boxN}$ is the size of $boxN$.

154 Last, to quantify the intensity of upwelling integrated over boxN and over the summer, we define the summer
155 upwelling index $UI_{JJAS,boxN}$ , computed over JJAS as:

156 $$UI_{JJAS,boxN} = \frac{\int_{JJAS} UI_{d,boxN}(t)dt}{ND_{JJAS}} \qquad (3)$$

157 where $ND_{JJAS}$ = 122 days is the JJAS duration.

158      **2.5. Indicators of OIV impact**

159 Following Waldman et al. (2018), we introduce two indicators to quantify the contribution of OIV on a given

160 variable $X$ : one at the daily scale and one at the average scale over a given period. $X(t,i)$ at time $t$ and for ensemble

161 member $i$ can be any time-dependent (space-dependent or not) variable characterizing the ocean circulation or

162 upwelling intensity. In the following, $\sigma_i$ is the ensemble standard deviation (that quantifies the time-dependent

163 intrinsic variability), $\sigma_t$ temporal standard deviation, $m_i$ the ensemble average and $m_t$ the temporal average.

164 We quantify the effect of OIV at the daily scale by computing $IV_d$, the contribution of intrinsic variability to the

165 total daily variability of $X(t,i)$. For each day of JJAS 2018, it is computed as the ratio between the time-dependent

166 intrinsic variability and the total temporal variability over JJAS 2018:

167 $$IV_d\big(X(t)\big) = \frac{\sigma_i\big(X(t,i)\big)}{\sqrt{m_i\big(\sigma_t\big(X(t,i)\big)^2\big)}} \qquad\qquad (6)$$

168 We quantify the contribution of OIV at the average scale over a given period by computing the relative intrinsic

169 variability of the temporal mean state of $X$ over the period, $IV_{tm}$. For that, we compute the ratio between the

170 ensemble standard deviation and the ensemble average of temporal average of $X(t,i)$:

171 $$IV_{tm}(X) = \frac{\sigma_i\big(m_t\big(X(t,i)\big)\big)}{m_i\big(m_t\big(X(t,i)\big)\big)} \qquad\qquad (5)$$

172 To investigate the effect of OIV on surface circulation and upwelling, we apply in the following those indicators

173 on the upwelling indices ($UI_d$, $UI_{d,boxN}$ and $UI_{JJAS,boxN}$) and on the surface current vorticity.

174      **3. Intraseasonal variability of wind and ocean circulation**

175 Figure 2 shows for each upwelling area the daily time series of wind stress, of $UI_{d,boxN}$ for each simulation and for

176 the ensemble average, and of $IV_d(UI_{d,boxN})$. The southwest summer monsoon wind blows from June to September

177 over the SCS with three main peaks of strong northeastward wind during mid-June, beginning to mid-July and

178 beginning of August, associated with three peaks of OFU, SCU and MKU that will be examined into details in

179 Section 4 (see the daily time series of $UI_{d,boxN}$ and wind stress averaged over boxOF, boxSC and boxMK, Figure

180 2a,b,c). To study the development of upwelling and the ocean circulation over those areas, we define three periods

181 that fully cover OFU development (from a value of UId,boxOF=0 to a maximum value) : June (9th-18th June, 10

182 days), July (28th June-18th July, 21 days) and August (1st-13th August, 13 days), highlighted in blue in Figure 2.

183 The development of OFU, SCU and MKU follows a similar chronology and the exact choice of each periods did

184 not modify our conclusions, as long as those periods cover the upwelling development and strong monsoon wind

185 periods. For the sake of readability and simplicity, we therefore use the three periods defined above for the

186 diagnostics used to study OFU, SCU and MKU. Figure 3a,b,c,d shows for each period the maps of ensemble

187 average of wind stress and wind stress curl, of surface current speed and of surface current vorticity averaged over

188 the period, and the maps of relative intrinsic variability ($IV_{tm}$) of surface current vorticity over the period. A high

189 (low) value of $IV_{tm}$ of current vorticity indicates a strong (weak) OIV and a chaotic (stable) circulation. To quantify

190 the strength of the eastward jet, we calculate the ensemble mean of the average surface current speed through the

191 meridional transect at 109.9°E, between 9.5 and 12.2°N (red line in Figure 3a) during the three periods.

During the June period, the area of strong positive wind stress curl extends from the coast to ~113°E, with a narrow meridional coverage (Figure 3a). The ACC dipole is not clearly formed (Figure 3b,c). The weak eastward jet is located in the south with a maximum speed of 0.5-0.7 m.s$^{-1}$ around 10-11°N, and a mean speed of 0.51 m.s$^{-1}$. The circulation is stable in the coastal jet area ($IV_{tm}$ of current vorticity <50%, Figure 3d), but much more chaotic over most of the offshore area ($IV_{tm}$ >200%). During the July period, the area of strong positive wind stress curl is larger than in June (from 10.5°N to 13°N, extending to 112°E). The eastward jet strengthens, with a mean speed of 0.78 m.s$^{-1}$, and is more in the north, with a speed of about 0.8-1.1m.s$^{-1}$ near 11-12°N. The ACC dipole, with an anticyclonic (cyclonic) circulation in the south (north), is more pronounced than in June. The circulation is more stable than in June in the coastal zone and in the cyclonic and anticyclonic areas ($IV_{tm}$ of current vorticity ~ 100%). It is less stable in the northeastern region of boxOF, where $IV_{tm}$ exceeds 200%. During the August period, the area of strong positive wind stress curl has the largest meridional and zonal extension, to 114°E. The eastward jet is still stronger, with velocities reaching 1.2-1.5 m.s$^{-1}$ around 10.5-11.5◦N and a mean speed up to 0.88 m.s$^{-1}$. The ACC dipole is also stronger, with a well-established and large cyclonic gyre. The surface circulation is more stable compared to June and July, with a larger area of low $IV_{tm}$ of current vorticity (<100%) covering boxOF. In September, the summer monsoon and the large-scale jet/ACC circulation begin to weaken (not shown).

## 4. Intraseasonal variability of upwelling

Here we examine the upwelling intraseasonal variability and its intrinsic variability for each upwelling area. Table 1 shows for the four areas the value of yearly upwelling index $UI_{JJAS,boxN}$ for each member and for the ensemble average, and its relative intrinsic variability $IV_{tm}$ $(UI_{JJAS,boxN})$. It also shows the values of the correlation coefficients between the daily time series of the ensemble mean of $UI_{d,boxN}$ and of the wind stress components and intensity. Figure 3e,f shows for each period defined in Section 3 the maps of $UI_d$ on the day of maximum $UI_{d,boxN}$ over each period and the maps of its relative intrinsic variability $IV_{tm}$ $(UI_d)$.

### 4.1. The southern coastal upwelling (SCU)

For SCU, $UI_{d,boxSC}$ time series show a similar daily chronology for each member and for the ensemble mean (Figure 2b). SCU begins to develop during the first half of June, lasts during the whole summer with a strong intraseasonal variability, and disappears during the first half of September. We obtain three peaks of similar intensity, near June 19th, July 15th and August 16th, in phase with the wind forcing over the area: the correlation between the time series of $UI_{d,boxSC}$ and of the daily averaged wind stress intensity over boxSC is equal to 0.64 (p<0.01, Table 1). The correlation with the wind stress eastward component, i.e. the component nearly parallel to the south coast, that favors the SCU, reaches 0.71 (p<0.01).

Over the summer, $IV_d$ $(UI_{d,boxSC})$ varies between 10% when SCU is weak and 40% during periods of strong SCU, showing similar values for the three upwelling peaks (Figure 2e). The yearly upwelling index $UI_{JJAS,boxSC}$ shows a weak ensemble standard deviation (7% relative to the mean, Table 1). This intrinsic variability of the SCU summer strength is much weaker than its interannual variability: in the 2009-2018 LONG simulation analyzed by To Duy et al. (2022), $UI_{JJAS,boxSC}$ shows a 53% interannual standard deviation relative to its interannual mean. SCU develops in the same area for the ten members, in the coastal zone of the ACC dipole convergence, as shown by

the very low values of $IV_{tm}$ ($UI_d$) (<50%) over this area (Figure 3e,f). Higher $IV_{tm}$ ($UI_d$) values are obtained at the periphery of this area, along the northern and southern flanks of the eastward jet. They are related to the variability of the meridional position of the jet: a jet located further north (south) induces a SCU further north (south).

SCU daily to intraseasonal variability is therefore mostly driven by the wind. The OIV is mainly related to the meridional position of the jet which does not vary much, thus affecting the SCU at a second order at the intraseasonal scale.

### 4.2. The Mekong delta shelf upwelling (MKU)

For MKU, time series of $UI_{d,boxMK}$ are almost identical for each member and for the ensemble mean (Figure 2c). They also show a strong intraseasonal variability, with three peaks of varying intensity following the three wind peaks. The July peak is the strongest, followed by the August peak, then the June peak. The daily chronology of MKU also strongly follows the wind chronology, with a correlation of 0.65 (p<0.01) with the wind stress intensity averaged over MKU, and of 0.59 (0.61) with the wind stress eastward (northward) component (Table 1).

MKU is very weakly influenced by the OIV: $IV_d$($UI_{JJAS,boxMK}$) never exceeds 30% (Figure 2e) and $IV_{tm}$ ($UI_{JJAS,boxMK}$) is equal to 6% (Table 1). Again, this intrinsic variability of MKU summer strength is negligible compared to its interannual variability: the interannual standard deviation of $UI_{JJAS,boxMK}$ is equal to 85% in the LONG simulation (To Duy et al., 2022). Spatially, MKU is also very stable. As shown by To Duy et al. (2022), it develops along the northeastward current, behind Con Dao islands (Figures 1, 3e). For the 3 periods of MKU development, Figure 3d,f shows extremely very weak values of $IV_{tm}$ both for the surface current vorticity and for the spatial upwelling index. The circulation is therefore extremely stable in this area, explaining the spatial stability of MKU.

The daily chronology and intensity of MKU are thus mainly driven by the wind, and its position is determined by non-varying factors, presumably bathymetry, that still need to be investigated, and not by chaotic factors like (sub)mesoscale circulation. As a result, MKU is almost not affected by OIV.

### 4.3. The offshore upwelling (OFU)

Again, the daily chronology of OFU is very similar for the ten members and the ensemble mean (Figure 2a), and in phase with the wind chronology (correlation of 0.65, p<0.01 with the daily wind stress intensity over boxOF, Table 1). However, contrary to SCU, the intensity of OFU peaks varies throughout the season, though wind stress intensity is similar during those peaks. We obtain two strong peaks (~1.0°C) in the heart of summer on July 19th and August 13th, a moderate peak (~0.6°C) at the end of August, and two small peaks (~0.2°C) at the beginning and end of summer, on June 18th and September 16th. $IV_d$($UI_{d,boxOF}$) also varies a lot seasonally, and is maximum and much stronger than for SCU and MKU during OFU peaks (Figure 2e): it reaches 90% for the July peak, 70% during the August peaks, and respectively 30% and 50% during the small June and September peaks. On the summer average, $IV_{tm}$ ($UI_{JJAS,boxOF}$) is equal to 18% (Table 1), again stronger than for SCU and MKU, but still much lower than the interannual variability (126%, To Duy et al., 2022). The regional daily wind stress therefore drives the daily to intraseasonal variability of OFU at the first order. However, OIV also significantly influences this daily variability, and this influence varies intraseasonally.

264    To understand the mechanisms that explain the intraseasonal variability of OFU intensity, we examine its

265    functioning during its three main periods of OFU development (June, July and August, highlighted in blue in

266    Figure 2). Da et al. (2019) and To Duy et al. (2022) showed that OFU is mainly induced by Ekman pumping and

267    develops in the area of strong positive wind stress curl and current vorticity. The eastward jet and ACC dipole

268    that favor the development of OFU are much stronger and well established in the heart of summer than at the

269    beginning and end of the summer monsoon (Figure 3bc and Part 3). Northeastward wind intensity is stronger in

270    July and August than in June and September (Figure 2) with a larger area of positive wind curl (Figure 3a).

271    Moreover, positive current vorticity developing in boxOF in the area of positive wind curl is much higher in July

272    and August, which further enhances Ekman pumping (Figure 3e). The intraseasonal variability of OFU peaks is

273    thus explained by the intraseasonal variability of wind and large-scale circulation.

274    We then examine the mechanisms that explain why the July and August peaks show different intrinsic variability

275    but similar ensemble mean of OFU intensity (Figure 2a). Figure 4a shows the maps of $UI_d$ on the day of maximum

276    $UI_{d,boxOF}$ over the July OFU development period and the maps of average surface current vorticity during the this

277    period for 2 members of strong OFU (13, maximum $UI_{d,boxOF}$ = 1.53 °C; 17, maximum $UI_{d,boxOF}$ = 1.42 °C, Figure

278    2a) and 2 members of weak OFU (15, maximum $UI_{d,boxOF}$ = 0.77 °C; 18, maximum $UI_{d,boxOF}$ = 0.65 °C). In July,

279    the eastward jet is much stronger than in June (Figure 3b,c and Section 3 above). OFU develops mainly in the

280    area of positive wind stress curl and current vorticity along the northern flank of the jet (Figures 3c,e and 4). When

281    the position of the eastward jet is located more to the south than average, as for members 13 and 17, the area of

282    positive current vorticity northern of the jet in BoxOF coincides with the area of positive wind curl. This

283    combination of positive current vorticity and positive wind curl enhances Ekman pumping induced upwelling

284    (Figure 4) and results in a strong OFU covering a large area. This is the opposite when the position of the eastward

285    jet is more to the north than average (members 15 and 18) : the area of positive current vorticity located in the

286    positive wind curl region is smaller, not enhancing the Ekman pumping induced upwelling (Figure 4). Figure 3d,f

287    shows strong values of $IV_{tm}$ of current vorticity and upwelling intensity (> 100%) along the eastward jet and in

288    the northeast area of boxOF. This confirms that OFU intrinsic variability in July is related to the effect of eastward

289    jet meridional position variability on the circulation and on the upwelling that develops along the northern flank

290    of the jet. Figure 4b shows the maps of $UI_d$ on the day of maximum $UI_{d,boxOF}$ over the August OFU development

291    period and the maps of average surface current vorticity and average wind stress curl during this period for 2

292    members of strong OFU (14, maximum $UI_{d,boxOF}$ = 1.65 °C; 13, maximum $UI_{d,boxOF}$ = 1.20 °C, Figure 2a) and 2

293    members of weak OFU (10, maximum $UI_{d,boxOF}$ = 0.82 °C; 16, maximum $UI_{d,boxOF}$ = 0.89 °C). In August, part of

294    OFU still develops in the area of positive surface current vorticity along the northern flank of the eastward jet, but

295    to less extent than in July (Figures 3e, 4). The meridional position of the jet does not vary a lot from one member

296    to another (Figure 4b), as confirmed by the lower values of $IV_{tm}$ of current vorticity in the jet area (Figure 3d).

297    The eastward jet is thus stronger and more stable than in July (Figure 3b,c and Part 3), and does not induce a

298    strong intrinsic variability of OFU. Instead, August OFU mainly develops in the area of positive vorticity north

299    of the jet associated with the cyclonic eddy of the ACC dipole (Figures 4b,3e). Variations of zonal position of this

300    eddy explain the variability of OFU intensity. From members 14, to 13, 10 and 16, this eddy is located more and

301    more to the east, i.e. further and further away from the area of strong positive wind stress curl, resulting in a

302    weaker and weaker OFU (Figures 4b). The variability of circulation in the northern part of boxOF therefore

303    explains OFU intrinsic variability in August. This variability is moreover lower than in July: $IV_{tm}$ of current

vorticity and of $UI_d$ in this northern part (highlighted by the black triangle in Figure 3d,e,f) is lower in August than in July. The more stable jet in August, that results in a smaller intrinsic variability of OFU along the jet, and smaller intrinsic variability of current vorticity in the northern cyclonic part, where OFU mostly develops, therefore explain the intrinsic variability of OFU in August and the fact that it is smaller than in July.

In OFU, MKU and SCU areas, the effect of intrinsic variability on $UI_d$ and the surface current vorticity therefore shows similar spatial patterns (Fig. 3d,f) and the influence of OIV on upwelling is directly linked to the influence of OIV on the circulation.

### 4.4. The northern coastal upwelling (NCU)

The ten members and the ensemble mean simulate NCU with a strong intraseasonal variability and a similar chronology (Figure 2d), completely different from the chronology obtained for the three other areas. A strong NCU develops at the beginning of summer (from June 10$^{th}$ to July 4$^{th}$, reaching ~1.2°C for the ensemble average), and a weak NCU develops at the end of August (August 26$^{th}$ to 31$^{st}$, reaching ~0.2°C). During those periods, highlighted in green in Figure 2, NCU chronology follows the wind chronology for the ten members: $UI_{d,boxNC}$ peaks correspond to peaks of northward (i.e. alongshore) wind favorable to NCU, around June 18$^{th}$ and 25$^{th}$, July 2$^{nd}$, and August 28$^{th}$ and 29$^{th}$. There still a significant correlation between the time series of $UI_{d,boxNC}$ and the time series of wind stress northward component over boxNC, that favors the Ekman upwelling in this area (0.37, p<0.01, Table 1). It is however much weaker than correlations obtained for the other areas (at least 0.64). Moreover, although northward wind peaks occur during the whole summer (e.g July 17$^{th}$ - 22$^{nd}$, highlighted in green in Figure 2) NCU does not develop from mid-July to mid-August.

NCU shows the strongest OIV of the four areas. $IV_d(UI_{d,boxNC})$ reaches 170% during the June-July peak, and is much smaller during the rest of the summer, reaching at most ~80% during the short late August peak (Figure 2e). The strong OIV in June explains the strong OIV at the summer scale (Table 1): $IV_{tm}(UI_{JJAS,boxNC})$ is equal to 37%, that is twice larger than for OFU and ~6 times larger than for SCU and MKU. It is twice smaller than the interannual variability of MKU summer strength (72% in the LONG simulation, To Duy et al., 2022).

These results suggest that the daily to intraseasonal chronology of upwelling in boxNC is partly driven by wind, but to less extent than in the other areas. Therefore other factors are involved that induce a strong intrinsic variability of NCU both at the daily and summer scales. To identify those factors, we use the three periods identified above : the period of strong wind over boxNC and strong NCU in June (June 10$^{th}$ – July 4$^{th}$), the period of strong wind but no NCU in July (July 17$^{th}$ - 22$^{nd}$), and the period of strong wind and weak NCU at the end of August (August 26$^{th}$ - 31$^{st}$). We show in Figure 5 the maps of ensemble average of average surface current, current vorticity and $IV_{tm}$ of current vorticity over each period, and the maps of $UI_d$ and $IV_{tm}(UI_d)$ on the day of maximum $UI_{d,boxNC}$ over each period.

During the June period, ensemble average circulation in and around boxNC is globally offshore oriented. This favors the Ekman transport, hence the development of NCU. The ensemble spreading of NCU strength is very strong: $IV_{tm}(UI_d)$ spatially exceeds 300% in the eastern part of boxNC (Figure 5e), and $IV_d(UI_{d,boxNC})$ reaches 170% (Figure 2e). Figure 6 shows the maps of wind speed and curl, current speed and vorticity and $UI_d$ on the day of maximum $UI_{d,boxNC}$ over the June period for two members of strong NCU (10 and 16) and two members of weak

341     NCU (09 and 11). A cyclonic gyre in the north and anticyclonic gyre in the south meet in boxNC for members 10

342     (between 13°N and 14°N) and 16 (between 14°N and 15°N). This induces a convergence and an offshore current

343     resulting in a strong upwelling, following the same mechanism as for SCU. For members 09 and 11, cyclonic and

344     anticyclonic gyres do not meet in boxNC, but either north or south of boxNC, not inducing offshore oriented

345     current over boxNC. Instead a weak NCU is induced by a favorable northward alongshore current in the northern

346     part of boxNC (Figure 6). As already observed at the interannual scale by To Duy et al. (2022) for the interannual

347     variability, mesoscale circulation of strongly chaotic nature in and around boxNC therefore drives the NCU

348     development and explains its high intrinsic variability during the June period. The effect of intrinsic variability on

349     NCU is not related to the intrinsic variability of current vorticity, but of current direction relative to the coast.

350     Between mid-July and mid-August, the large-scale circulation (ACC dipole and eastward jet) is strongly

351     established (see Section 3). The western part of the cyclonic eddy covers boxNC and induces a strong southward

352     alongshore current over this region. Close to the coast, this alongshore current is associated with a divergent

353     circulation, hence with a coastward component and a coastal downwelling which inhibits the NCU (see the high

354     negative vorticity in this area during the July period in Figure 5b). This large-scale ocean circulation is common

355     for the ten members and systematically prevents the NCU to develop (see the weak $IV_{tm}$ of current vorticity and

356     the weak upwelling in Figure 5). This explains the very weak $UI_{d,boxNC}$ and $IV_d(UI_{d,boxNC})$ during this period (Figure

357     2e).

358     During the August period, the average circulation is similar to the mid-July and mid-August circulation described

359     above (Figure 5a,b). However, with the weakening of the summer monsoon, the ACC dipole structure

360     progressively weakens, the negative vorticity is less strong and the current is a bit more offshore oriented: NCU

361     is not as strong as in June, but it can develop easier than in the middle of the summer. $IV_d(UI_{d,boxNC})$ consequently

362     increases, but stays smaller than in June.

363     Our results therefore show that the development of NCU at the intraseasonal scale is first related to the large-scale

364     circulation, which prevents it during the heart of summer and allows it at the beginning and end of summer. Inside

365     those periods of "allowed NCU development", it is first driven by wind, then by the mesoscale circulation that

366     explains its very strong intrinsic variability.

367     **5. Conclusion and future work**

368     An ensemble of ten fine-resolution simulations with perturbed initial conditions was performed and analyzed in

369     this paper to represent and investigate the daily to intraseasonal variability of ocean circulation and of SVU over

370     its different areas of development and the influence of OIV.

371     The ensemble was used to examine the seasonal variability and intrinsic variability of the circulation in the SVU

372     region during summer 2018. In June, the eastward jet is weak and mainly located in the south, the ACC dipole is

373     not formed and the circulation is only stable in the coastal area. In July, the jet is stronger and the ACC dipole is

374     clearly formed. The circulation in the area of positive vorticity north of the jet is more stable. In August southwest

375     monsoon wind is the strongest and has the largest area of influence, inducing an even stronger eastward jet and a

376     pronounced ACC dipole. In August, the circulation is stable over a larger area than in July.

377     We then examined the seasonal variability and intrinsic variability of the upwelling.

For SCU, MKU and OFU, the daily chronology and intraseasonal variability of the upwelling are quite similar and mainly driven by the summer monsoon wind, with upwelling maxima in phase with strong southwest wind periods. Their intrinsic variability is much weaker than their interannual variability.

The development of MKU and SCU is related to ocean circulation processes, respectively the northeastward current and eastward jet, that are spatially quite stable. As a result, MKU and SCU show a very weak (less than 10%) intrinsic variability in space and time, both at daily scale and on average over summer. Peaks of OIV are related to peaks of upwelling intensity. SCU develops as long as wind conditions are favorable over the area of the ACC dipole convergence, that does not vary much spatially. MKU develops along the northeastward current that flows offshore the Mekong delta and is spatially very stable.

OFU shows stronger intrinsic variability (18%), both at daily scale and for the whole summer period, and also in space. The seasonal variability of OFU intensity and intrinsic variability are not only driven by the wind, but also related to the period of the season. The large-scale circulation (ACC dipole and eastward jet) that enhances the Ekman pumping – induced OFU is weak in June and September, whereas it is strongly established in the heart of summer in July and August. This explains the stronger OFU intensity and OIV during the July-August period. Moreover, for similar OFU intensity, the impact of OIV is weaker in August than in July. In July, OFU mainly develops along the northern flank of the eastward jet. The meridional position of this jet is quite variable, explaining the strong intrinsic variability of the July OFU: a southern (northern) position of the jet induces a larger (smaller) common area between positive curl of wind stress and current, hence induces a stronger (weaker) upwelling. In August, this position is much more stable. Moreover, OFU mainly develops in the area of cyclonic activity north of the jet, related to mesoscale eddies of strong chaotic nature. OFU intensity depends on the zonal position of this cyclonic activity with respect to the wind curl: a cyclonic eddy (not) located in the area of strong positive wind stress curl results in stronger (weaker) OFU. The circulation in this area is moreover more stable than in July, explaining the weaker intrinsic variability in August.

NCU daily chronology and the intraseasonal variability is completely different from that found in the three other areas, and its intrinsic variability is much higher. At the intraseasonal scale, the development of NCU is driven by the large-scale circulation. During the heart of summer, from mid-July to end of August, the eastward jet and ACC dipole are strongly established, inducing a strong southward alongshore current over boxNC which annihilates NCU, explaining its very low intensity and intrinsic variability. At the beginning and, to less extent, end of summer, the large-scale ACC dipole structure and associated eastward current are weaker, allowing offshore current to develop. Inside these periods, NCU chronology is driven by the wind but also by the development (or not) of offshore oriented currents related to the spatial organization of coastal eddies. NCU shows a strong intrinsic variability related to strong chaotic variability of mesoscale structures with the order of magnitude similar to interannual variability (37%).

We investigated here the effect of OIV on the circulation and upwelling in the SVU region, confirming that this chaotic part of ocean variability here is mainly related to the small-scale structures, as previously shown for other and larger areas. Following this study as well as those of Da et al. (2019) and To Duy et al. (2022), we can draw some perspectives on the application of research regarding the predictability of SVU at the intraseasonal to interannual scale. The development of MKU and SCU, which is little affected by OIV, could be largely predicted

416 using wind forecasts, provided of course that these forecasts are reliable. At first order, OFU can be partially
417 predicted from wind forecasts, but with uncertainties in its daily to summer integrated magnitude that can vary by
418 a factor of 1.5 to 2 (see Figure 2 and Table 1). Wind forecasts could identify favorable/unfavorable periods for
419 NCU development. However, favorable periods would be associated with a high uncertainty rate in terms of NCU
420 intensity, given the strong impact of OIV on NCU during these periods. Further studies are underway to investigate
421 the influence of other factors, including rivers and tides. Chen et al. (2012) indeed suggested that tides could
422 influence the SVU development. Tidal amplitude is particularly strong over the shallow Mekong shelf region
423 (Phan et al. 2019), moreover submitted to the influence of the Mekong river waters. Both factors may therefore
424 affect SVU development and variability, in particular over the MKU and SVU areas. We moreover developed an
425 ocean-atmosphere regional coupled model that will allow to study the impact of upwelling on atmosphere and
426 climate, at local and regional scales, that was studied until now using satellite data and an atmosphere-only model
427 (Xie et al. 2003; Zheng et al., 2016; Yu et al., 2020). The impact of upwelling on the marine ecosystem should
428 also be studied, using for example the dynamical-biogeochemical coupled model developed by Ulses et al. (2016)
429 and Herrmann et al. (2017). Finally, the long-term evolution of the upwelling should be studied, in particular since
430 Herrmann et al. (2020,2022) showed that summer monsoon winds may weaken in response to climate change.
431 Last, the upwelling that develops offshore the Mekong Delta, MKU, was revealed by To Duy et al. (2022) and
432 confirmed by the present study, and the northern coastal upwelling, NCU, was revealed by Da et al. (2019) and
433 confirmed by Ngo and Hsin (2021). Extremely few in-situ observations are available over these two areas, and
434 field campaigns are therefore necessary to better understand their functioning. This study explored the impact of
435 OIV on the South Vietnam Upwelling, but is more generally of interest for the scientific community working on
436 the functioning and variability of upwellings and on the effect and modeling of OIV.

437

**Code and data availability**

439 The SYMPHONIE model is available on the webpage of the SIROCCO group, https://sirocco.obs-mip.fr/. Sea
440 surface temperature, currents and windstress simulated by the ensemble over summer 2018 are freely available
441 on https://doi.org/10.5281/zenodo.7504087.

442

**Authors Contribution**

444 Marine Herrmann, To Duy Thai and Claude Estournel designed the experiments and To Duy Thai carried them
445 out. Marine Herrmann prepared the manuscript with contributions from all co-authors.

446

**Competing interests**

448 The authors declare that they have no conflict of interest.

449

**Acknowledgements**

451    This work is a part of LOTUS international joint laboratory (lotus.usth.edu.vn). PhD studies of To Duy Thai were

452    funded through an IRD ARTS grant and a "Bourse d'Excellence" from the French Embassy in Vietnam.

453    Numerical simulations were performed using CALMIP HPC facilities (project P13120) and the cluster OCCIGEN

454    from the CINES group (project DARI A0080110098). This paper is a contribution to celebrate the 100 years

455    Anniversary of the Institute of Oceanography, Vietnam Academy of Science and Technology. The authors warmly

456    thank both reviewers for their constructive comments.

457

458

459 **Tables**

460 Table 1 : For each upwelling area: value of the yearly upwelling index $UI_{JJAS,boxN}$ for each member of the ensemble,

461 of the ensemble mean $mi(UI_{JJAS,boxN})$ and of $IV_{tm}(UI_{JJAS,boxN})$, and correlation coefficients between the daily times

462 series of the ensemble mean of the daily upwelling index $UI_{d,boxN}$ and of the wind stress eastward and northward

463 components and intensity. Only correlations associated with p-values <0.01 are shown.

| Members | 09 | 10 | 11 | 12 | 13 | 14 | 15 | 16 | 17 | 18 | $m_i(UI_{JJAS,boxN})$ (°C) | $IV_{tm}(UI_{JJAS,boxN})$ (%) | Correlation between $m_i(UI_{d,boxN})$ and wind stress eastward component | Correlation between $m_i(UI_{d,boxN})$ and wind stress northward component | Correlation between $m_i(UI_{d,boxN})$ and wind stress intensity |
|---------|------|------|------|------|------|------|------|------|------|------|------|------|------|------|------|
| BoxOF | 0.32 | 0.35 | 0.26 | 0.39 | 0.37 | 0.39 | 0.26 | 0.26 | 0.42 | 0.31 | 0.33 | 18 % | 0.62 | 0.62 | 0.65 |
| BoxSC | 1.25 | 1.35 | 1.25 | 1.49 | 1.39 | 1.42 | 1.27 | 1.38 | 1.48 | 1.29 | 1.36 | 7 % | 0.60 | 0.71 | 0.64 |
| BoxNC | 0.11 | 0.24 | 0.08 | 0.15 | 0.17 | 0.14 | 0.25 | 0.25 | 0.26 | 0.13 | 0.18 | 37 % | -- | 0.37 | -- |
| BoxMK | 0.18 | 0.18 | 0.19 | 0.19 | 0.17 | 0.18 | 0.17 | 0.18 | 0.2 | 0.17 | 0.18 | 6 % | 0.59 | 0.61 | 0.65 |

464
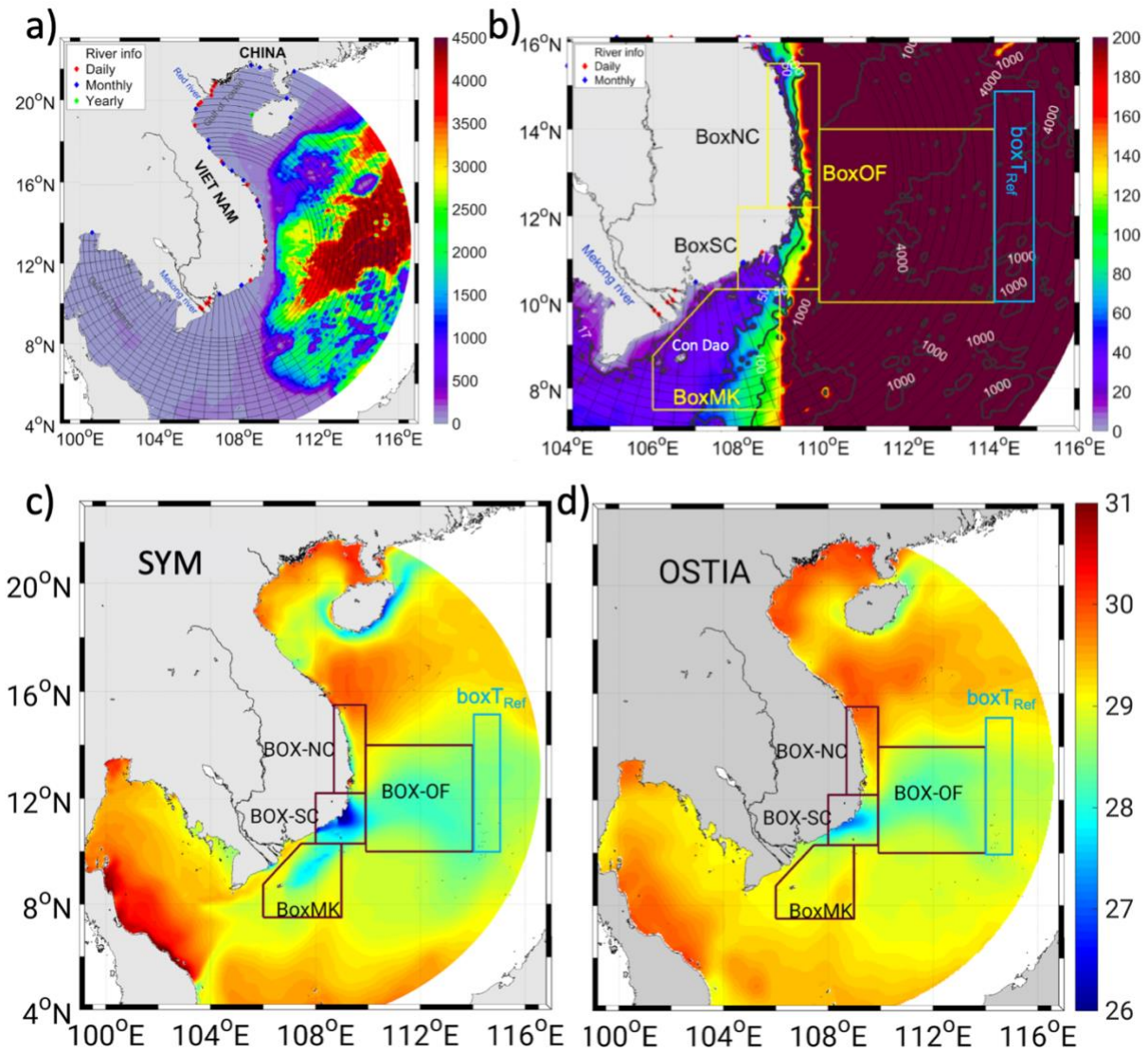
 **Figures**

Figure 1: (a) Characteristics of the orthogonal curvilinear computational grid (black lines, not all the mesh points are shown for visibility purposes) and bathymetry (colors, meter, *GEBCO_2014*) used for the VNC configuration of the SYMPHONIE model. Dots show the location of rivers for which we used daily (red), monthly (blue) and yearly climatology (green) discharge values (see To Duy et al. 2022 for more details). (b) Bathymetry (meter) over the SVU region. The 4 boxes used for the study of SVU are displayed in yellow. $boxT_{Ref}$ is highlighted in blue. (c,d) SST (°C) averaged over JJAS 2018 computed from the SYMPHONIE ensemble average (c) and from OSTIA reanalysis (d).

478
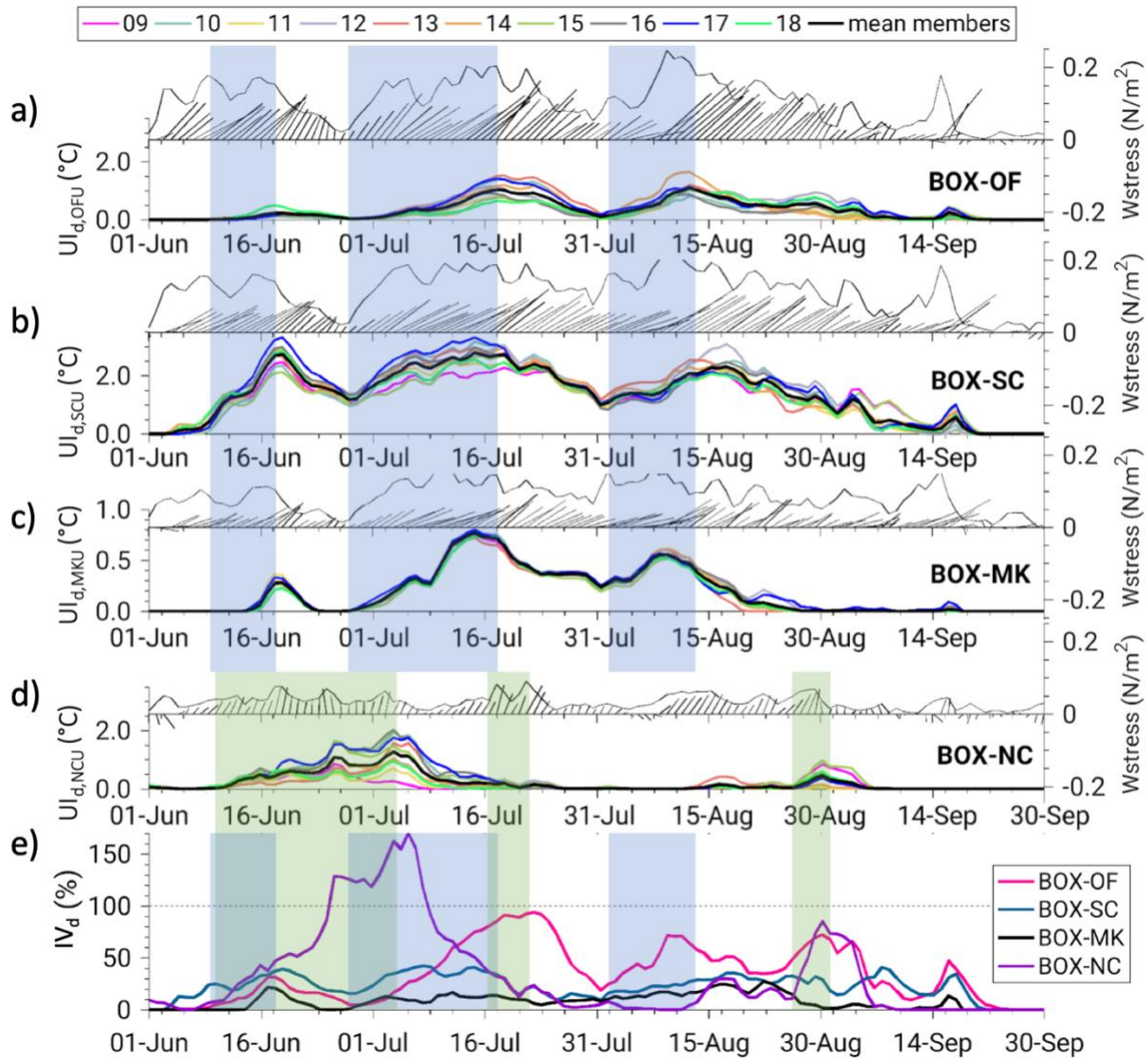
Figure 2: (a,b,c,d) Daily time series between June 1$^{st}$ and September 30$^{th}$ 2018 of direction (arrows) and intensity (black line) of spatially averaged wind stress (N.m$^{-2}$) over each upwelling area, and time series of $UI_{d,boxN}$ for each simulation (colored lines) and for the ensemble average (black thick line) for each upwelling area (a, BoxSC; b, BoxOF; c, BoxMK; d, BoxNC). (e) Daily time series of $IV_d(UI_{d,boxN})$ for each upwelling area. Periods covering OFU, SCU and MKU development are highlighted in blue. Periods used to study MKU development are highlighted in green.

485

486
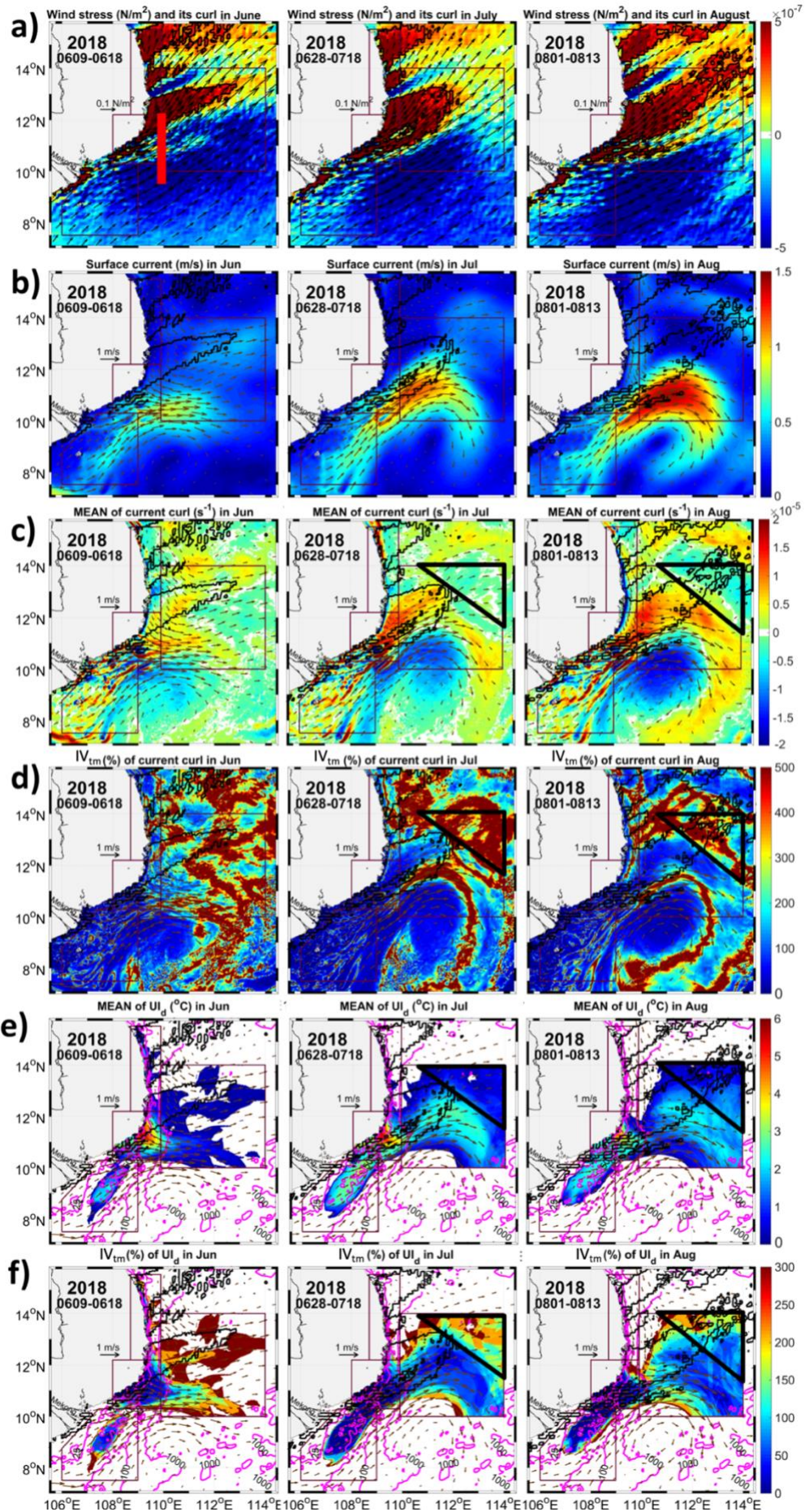
487    Figure 3: Maps of ensemble average of average wind stress (a, arrows, $N.m^{-2}$) and wind stress curl (a, colors, $N.m^{-3}$), of average surface current speed (b, $m.s^{-1}$) and vorticity (c, $s^{-1}$), of $UI_d$ (e, °C) on the day of maximum $UI_{d,boxOF}$
488
489    over each period of OFU development highlighted in blue in Figure 2 (left June, middle July and right August),
490    and maps of relative intrinsic variability ($IV_{tm}$) of average surface current vorticity (d, %) and of $UI_d$ (f, %) over
491    each period. Black lines: $3.10^{-7}$ $N.m^{-3}$ iso-contours of average wind stress curl. Red segment (a): meridional
492    transect at 109.9°E, 9.5 - 12.2°N used to compute the eastward jet strength. Arrows (b-f): average surface current
493    during each period. Black triangles (c-f): area of high current vorticity northern of the eastward jet during the July
494    and August periods. Pink lines (e, f): isobaths (meters).

495
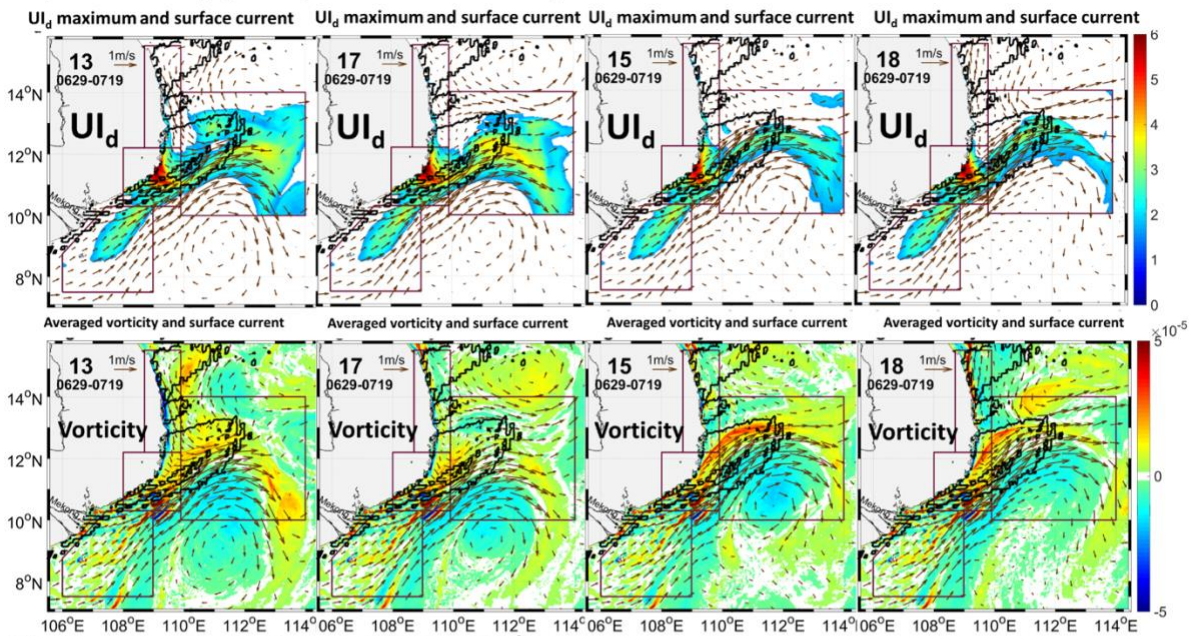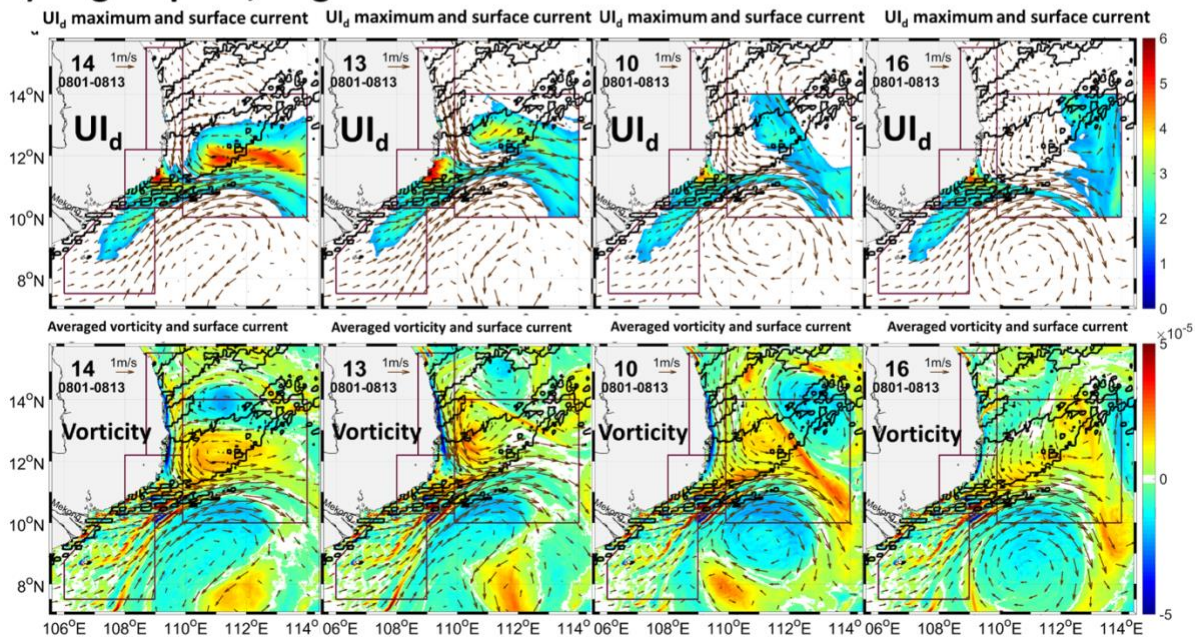
Figure 4: Maps of $UI_d$ (top, °C) on the day of maximum $UI_{d,boxOF}$ over the periods of OFU development (highlighted in blue in Figure 2) in (a) July and (b) August, and of average surface current vorticity (bottom, $s^{-1}$) during each period for 2 members of strong OFU (members 13 and 17 for July, members 14 and 13 for August, Figure 2a) and 2 members of weak OFU (members 15 and 18 for July, members 10 and 16 for August). Black contours: $3.10^{-7}$ N.m$^{-3}$ iso-contours of average wind stress curl during each period. Arrows: average surface current (m.s$^{-1}$).

505

506

507
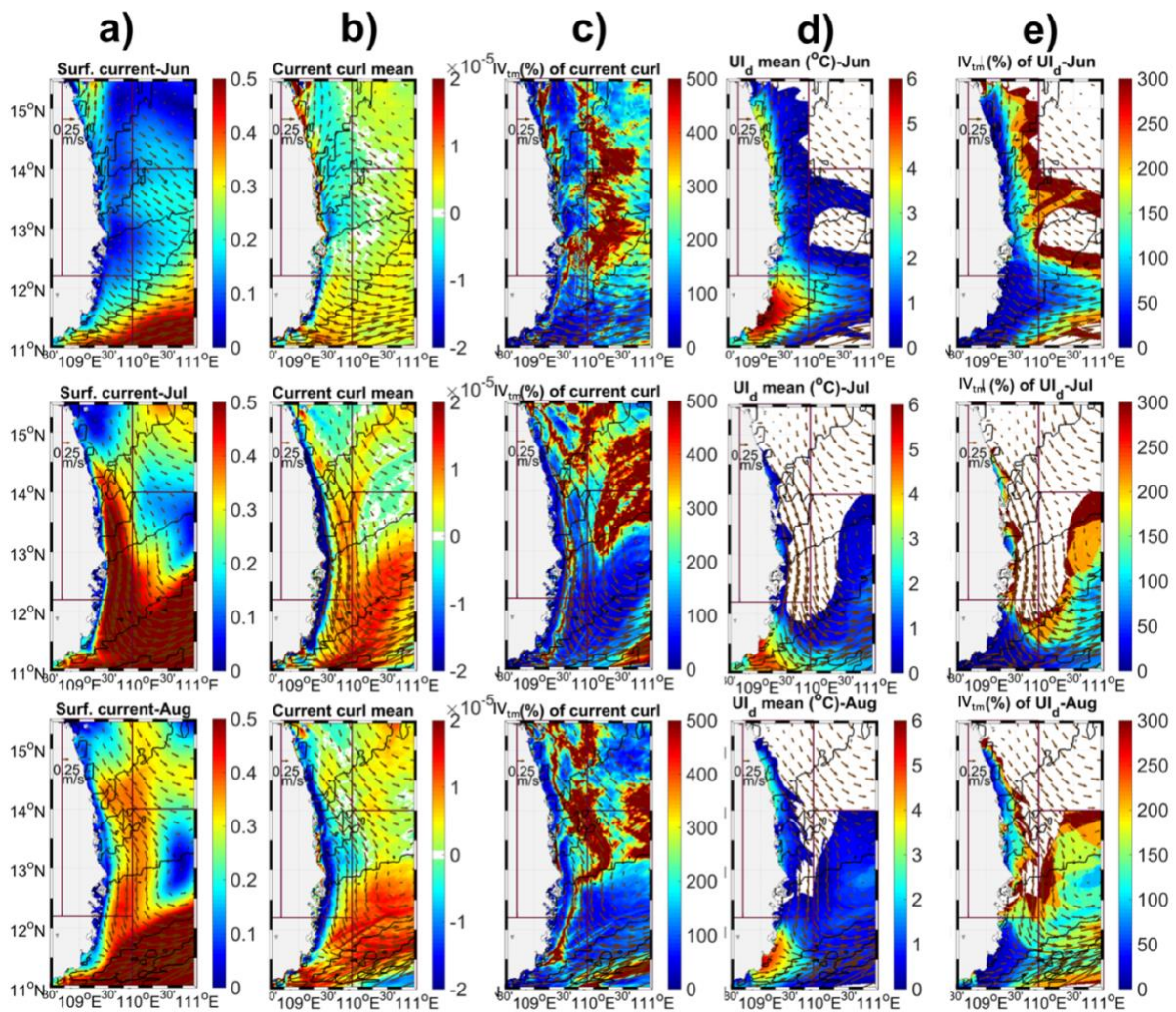
Figure 5 : Maps of ensemble average of average surface current speed (a, m.s⁻¹) and vorticity (b, s⁻¹) over each wind peak period over BoxNC (highlighted in green in Figure 2: 1$^{st}$ row June 10$^{th}$ – July 4$^{th}$, 2$^{nd}$ row July 17$^{th}$ - 22$^{nd}$ and 3$^{rd}$ row August 26$^{th}$ - 31$^{st}$), of $UI_d$ (d, °C) on the day of maximum $UI_{d,boxNC}$ over each period, and of relative intrinsic variability $IV_{tm}$ of average surface current vorticity (c, %) and $UI_d$ (e, %) over each period. Black contours: 3.10⁻⁷ N.m⁻³ iso-contours of average wind stress curl during each period. Arrows: average surface current (m.s⁻¹).

514

515

516
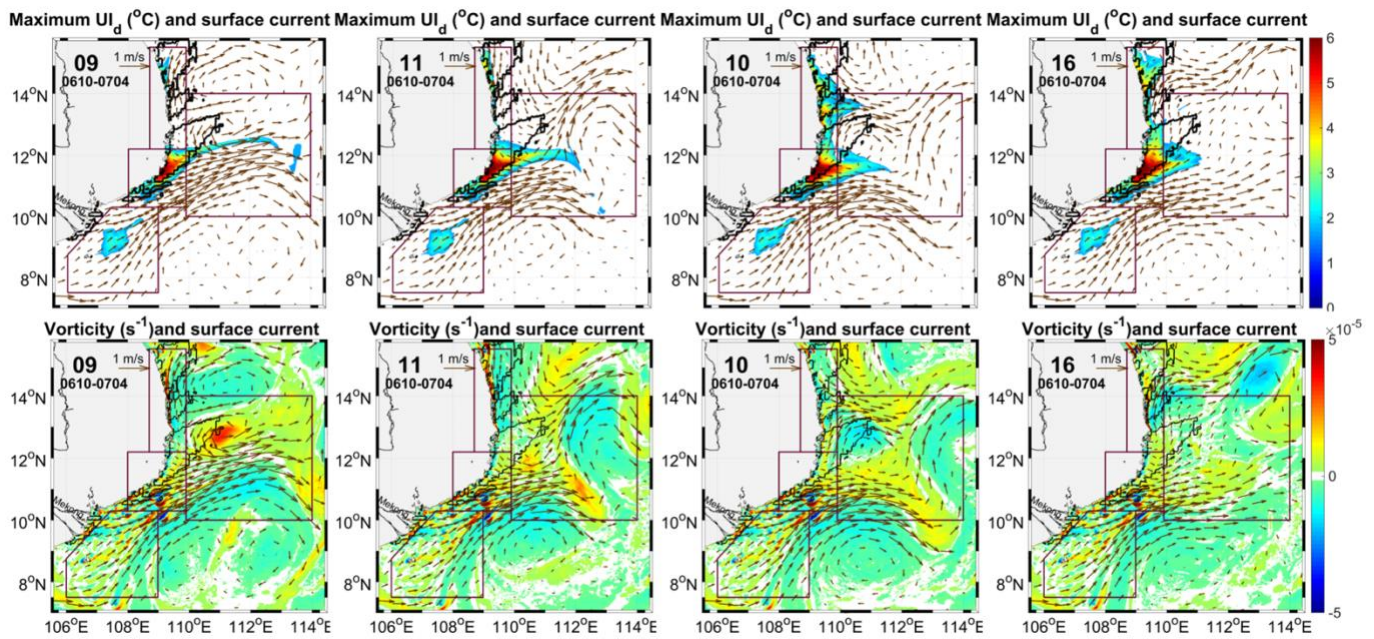
Figure 6 : Maps of $UI_d$ (1st row, °C) on the day of maximum $UI_{d,boxNC}$ over the July wind peak period over BoxNC (highlighted in green in Figure 2) and maps of average surface current vorticity (2nd row, s⁻¹) for 2 members of weak NCU (9, 11) and 2 members of strong NCU (10, 16) during the June-July period. Black contours: 3.10⁻⁷ N.m⁻³ iso-contours of average wind stress curl during each period. Arrows: average surface current (m.s⁻¹).

521

522    References

523    Bombar, D., Dippner, J. W., Doan, H. N., Ngoc, L. N., Liskow, I., Loick-Wilde, N., and Voss, M.: Sources of
524        new nitrogen in the Vietnamese upwelling region of the South China Sea, J. Geophys. Res. Ocean., 115, 6018,
525        https://doi.org/10.1029/2008JC005154, 2010.

526    Chen, C. and Wang, G.: Interannual variability of the eastward current in the western South China Sea associated
527        with the summer Asian monsoon, J. Geophys. Res. Ocean., 119, 5745–5754,
528        https://doi.org/10.1002/2014JC010309, 2014.

529    Chen, C., Lai, Z., Beardsley, R. C., Xu, Q., Lin, H., and Viet, N. T.: Current separation and upwelling over the
530        southeast shelf of Vietnam in the South China Sea, J. Geophys. Res. Ocean., 117, 1–16,
531        https://doi.org/10.1029/2011JC007150, 2012.

532    Da, N. D., Herrmann, M., Morrow, R., Niño, F., Huan, N. M., and Trinh, N. Q.: Contributions of Wind, Ocean
533        Intrinsic Variability, and ENSO to the Interannual Variability of the South Vietnam Upwelling: A Modeling
534        Study, J. Geophys. Res. Ocean., 124, 6545–6574, https://doi.org/10.1029/2018JC014647, 2019.

535    Dippner, J. W., Nguyen, K. V., Hein, H., Ohde, T., and Loick, N.: Monsoon-induced upwelling off the Vietnamese
536        coast, Ocean Dyn., 57, 46–62, https://doi.org/10.1007/S10236-006-0091-0, 2007.

537    Herrmann, M., Auger, P. A., Ulses, C., and Estournel, C.: Long-term monitoring of ocean deep convection using
538        multisensors altimetry and ocean color satellite data, J. Geophys. Res. Ocean., 122, 1457–1475,
539        https://doi.org/10.1002/2016JC011833, 2017.

540    Herrmann, M., Ngo-Duc, T., and Trinh-Tuan, L.: Impact of climate change on sea surface wind in Southeast Asia,
541        from climatological average to extreme events: results from a dynamical downscaling, Clim. Dyn. 2020 543,
542        54, 2101–2134, https://doi.org/10.1007/S00382-019-05103-6, 2020.

543    Herrmann, M., Nguyen-Duy, T., Ngo-Duc, T., and Tangang, F.: Climate change impact on sea surface winds in
544        Southeast Asia, Int. J. Climatol., 42, 3571–3595, https://doi.org/10.1002/JOC.7433, 2022.

545    Isoguchi, O., and Kawamura, H.: MJO-related summer cooling and phytoplankton blooms in the South China Sea
546        in recent years, Geophys. Res. Lett., 33, L16615, doi:10.1029/2006GL027046, 2006.

547    Kuo, N. J., Zheng, Q., and Ho, C. R.: Response of Vietnam coastal upwelling to the 1997-1998 ENSO event
548        observed by multisensor data, Remote Sens. Environ., 89, 106–115, https://doi.org/10.1016/j.rse.2003.10.009,
549        2004.

550    Li, Y., Han, W., Wilkin, J. L., Zhang, W. G., Arango, H., Zavala-Garay, J., Levin, J., and Castruccio, F. S.:
551        Interannual variability of the surface summertime eastward jet in the South China Sea, J. Geophys. Res.
552        Ocean., 119, 7205–7228, https://doi.org/10.1002/2014JC010206, 2014.

553    Liu, X., Wang, J., Cheng, X., and Du, Y.: Abnormal upwelling and chlorophyll-a concentration off South Vietnam
554        in summer 2007, J. Geophys. Res. Ocean., 117, 2–11, https://doi.org/10.1029/2012JC008052, 2012.

555    Loick-Wilde, N., Bombar, D., Doan, H. N., Nguyen, L. N., Nguyen-Thi, A. M., Voss, M., and Dippner, J. W.:
556        Microplankton biomass and diversity in the Vietnamese upwelling area during SW monsoon under normal
557        conditions and after an ENSO event, Prog. Oceanogr., 153, 1–15,
558        https://doi.org/10.1016/j.pocean.2017.04.007, 2017.

559    Lu, W., Oey, L. Y., Liao, E., Zhuang, W., Yan, X. H., and Jiang, Y.: Physical modulation to the biological
560        productivity in the summer Vietnam upwelling system, Ocean Sci., 14, 1303–1320,
561        https://doi.org/10.5194/OS-14-1303-2018, 2018.

Lyard, F., Lefevre, F., Letellier, T., and Francis, O.: Modelling the global ocean tides: modern insights from FES2004, Ocean Dyn. 2006 565, 56, 394–415, https://doi.org/10.1007/S10236-006-0086-X, 2006.

Marsaleix, P., Auclair, F., Floor, J. W., Herrmann, M. J., Estournel, C., Pairaud, I., and Ulses, C.: Energy conservation issues in sigma-coordinate free-surface ocean models, Ocean Model., 20, 61–89, https://doi.org/10.1016/j.ocemod.2007.07.005, 2008.

Marsaleix, P., Michaud, H., and Estournel, C.: 3D phase-resolved wave modelling with a non-hydrostatic ocean circulation model, Ocean Model., 136, 28–50, https://doi.org/10.1016/J.OCEMOD.2019.02.002, 2019.

Ngo, M. H. and Hsin, Y. C.: Impacts of Wind and Current on the Interannual Variation of the Summertime Upwelling Off Southern Vietnam in the South China Sea, J. Geophys. Res. Ocean., 126, e2020JC016892, https://doi.org/10.1029/2020JC016892, 2021.

Pairaud, I., Lyard, F., Auclair, F., Letellier, T., and Marsaleix, P.: Dynamics of the semi-diurnal and quarter-diurnal internal tides in the Bay of Biscay. Part 1: Barotropic tides, Cont. Shelf Res., 28, 1294–1315, https://doi.org/10.1016/J.CSR.2008.03.004, 2008.

Pairaud, I., Staquet, C., Sommeria, J., and Mahdizadeh, M. M.: Generation of harmonics and sub-harmonics from an internal tide in a uniformly stratified fluid: Numerical and laboratory experiments, 28, 51–62, https://doi.org/10.1007/978-94-007-0360-5_5/COVER/, 2010.

Penduff, T., Juza, M., Barnier, B., Zika, J., Dewar, W. K., Treguier, A. M., Molines, J. M., and Audiffren, N.: Sea level expression of intrinsic and forced ocean variabilities at interannual time scales, Journal of Climate, 24, 5652–5670. https://doi.org/10.1175/JCLI-D-11-00077.1, 2011

Phan, H. M., Ye, Q., Reniers, A. J.H.M., Stive, M. J. F: Tidal wave propagation along The Mekong deltaic coast, Estuarine, Coastal and Shelf Science, 220, 73-98, https://doi.org/10.1016/j.ecss.2019.01.026; 2019

Sérazin, G., Meyssignac, B., Penduff, T., Terray, L., Barnier, B., and Molines, J. M.: Quantifying uncertainties on regional sea level change induced by multidecadal intrinsic oceanic variability, Geophys. Res. Lett., 43, 8151–8159, https://doi.org/10.1002/2016GL069273, 2016.

To Duy, T., Herrmann, M., Estournel, C., Marsaleix, P., Duhaut, T., Bui Hong, L., and Trinh Bich, N.: Role of wind, mesoscale dynamics and coastal circulation in the interannual variability of South Vietnam Upwelling, South China Sea. Answers from a high resolution ocean model, Ocean Sci., 18, 1131–1161, https://doi.org/10.5194/os-18-1131-2022, 2022

Ulses, C., Auger, P. A., Soetaert, K., Marsaleix, P., Diaz, F., Coppola, L., Herrmann, M. J., Kessouri, F., and Estournel, C.: Budget of organic carbon in the North-Western Mediterranean open sea over the period 2004–2008 using 3-D coupled physical-biogeochemical modeling, J. Geophys. Res. Ocean., 121, 7026–7055, https://doi.org/10.1002/2016JC011818, 2016.

Waldman, R., Herrmann, M., Somot, S., Arsouze, T., Benshila, R., Bosse, A., Chanut, J., Giordani, H., Sevault, F. and Testor, P.: Impact of the Mesoscale Dynamics on Ocean Deep Convection: The 2012-2013 Case Study in the Northwestern Mediterranean Sea, J. Geophys. Res. Oceans., 122, 8813– 8840, doi:10.1002/2016JC01258, 2017b.

Waldman, R., Somot, S., Herrmann, M., Sevault, F., and Isachsen, P. E.: On the Chaotic Variability of Deep Convection in the Mediterranean Sea, Geophys. Res. Lett., 45, 2433–2443, https://doi.org/10.1002/2017GL076319, 2018.

Waldman, R., Somot, S., Herrmann, M., Bosse, A., Caniaux, G., Estournel, C., Houpert, L., Prieur, L., Sevault, F., and Testor, P.: Modeling the intense 2012–2013 dense water formation event in the northwestern

603    Mediterranean Sea: Evaluation with an ensemble simulation approach, J. Geophys. Res.
604    Oceans, 122, 1297– 1324, doi:10.1002/2016JC012437, 2017a.

605    Wang, B., LinHo, Zhang, Y., and Lu, M. M.: Definition of South China Sea monsoon onset and commencement
606    of the East Asian summer monsoon, J. Clim., 17, 699–710, https://doi.org/10.1175/2932.1, 2004.

607    Wang, Y., Fang, G., Wei, Z., Qiao, F., and Chen, H.: Interannual variation of the South China Sea circulation and
608    its relation to El Niño, as seen from a variable grid global ocean model, J. Geophys. Res. Ocean., 111, 1–15,
609    https://doi.org/10.1029/2005JC003269, 2006.

610    Wyrtki, K.: Physical oceanography of the South East Asian Waters, Naga Rep., 2, 1961.

611    Xie, S.-P., Xie, Q., and Wang, D.: Summer Upwelling in the South China Sea and its Role in Regional Climate
612    Variations, J. Geophys. Res., 108, 1–37, https://doi.org/10.1029/2003JC001867, 2003.

613    Xie, S. P., Chang, C. H., Xi, Q., and Wang, D.: Intraseasonal variability in the summer South China Sea: Wind
614    jet, cold filament, and recirculations, J. Geophys. Res. Ocean., 112, 1–11,
615    https://doi.org/10.1029/2007JC004238, 2007.

616    Yu, Y., Wang, Y., Cao, L., Tang, R. and Chai, F.: The ocean-atmosphere interaction over a summer upwelling
617    system in the South China Sea, Journal of Marine Systems, 208, 103360,
618    https://doi.org/10.1016/j.jmarsys.2020.103360, 2020.

619    Zheng, Z. W., Zheng, Q., Kuo, Y. C., Gopalakrishnan, G., Lee, C. Y., Ho, C. R., Kuo, N. J., and Huang, S. J.:
620    Impacts of coastal upwelling off east Vietnam on the regional winds system: An air-sea-land interaction, Dyn.
621    Atmos. Ocean., 76, 105–115, https://doi.org/10.1016/j.dynatmoce.2016.10.002, 2016.